

Article

# COVID-19 Image Classification: A Comparative Performance Analysis of Hand-Crafted vs. Deep Features

Sadiq Alinsaif 

College of Computer Science and Engineering, University of Hafr Al Batin, Hafar Al Batin 39524, Saudi Arabia; alinsaif@uhb.edu.sa

**Abstract:** This study investigates techniques for medical image classification, specifically focusing on COVID-19 scans obtained through computer tomography (CT). Firstly, handcrafted methods based on feature engineering are explored due to their suitability for training traditional machine learning (TML) classifiers (e.g., Support Vector Machine (SVM)) when faced with limited medical image datasets. In this context, I comprehensively evaluate and compare 27 descriptor sets. More recently, deep learning (DL) models have successfully analyzed and classified natural and medical images. However, the scarcity of well-annotated medical images, particularly those related to COVID-19, presents challenges for training DL models from scratch. Consequently, I leverage deep features extracted from 12 pre-trained DL models for classification tasks. This work presents a comprehensive comparative analysis between TML and DL approaches in COVID-19 image classification.

**Keywords:** machine learning; deep learning; convolutional neural networks; deep features; COVID-19; classification; CT scan

## 1. Introduction

Coronavirus disease 2019 (COVID-19) poses a significant global health threat due to its highly contagious nature, primarily transmitted through respiratory droplets expelled during coughing, sneezing, or speaking [1,2]. This respiratory illness represents one of the most lethal infectious diseases of our time [3], often leading to a substantial decline in the quality of life for afflicted individuals [4]. While the standard diagnostic tool, reverse transcriptase-polymerase chain reaction (RT-PCR), is widely employed, its limitations include a non-negligible rate of false negative results [5]. Therefore, developing and exploring alternative methodologies for accurate COVID-19 diagnosis is crucial.

Chest computed tomography (CT) [6] has emerged as a valuable adjunct to RT-PCR testing in the context of COVID-19 screening and diagnosis. Studies such as those by Fang et al. [7] and Ai et al. [8] have demonstrated the efficacy of CT scans in identifying COVID-19 patients with high sensitivity, even in cases where initial RT-PCR results were negative. This suggests the potential benefit of utilizing CT scans, particularly for patients exhibiting suggestive clinical symptoms despite negative RT-PCR findings [7].

Manual analysis of COVID-19 chest CT scans by radiologists presents a time-consuming burden, especially in emergency settings with high patient volumes. This necessitates the development of robust computer-aided diagnosis (CAD) systems capable of leveraging the rich information embedded within digital CT scans. Machine learning (ML) frameworks, in conjunction with image processing techniques, offer promising avenues for the construction of such CAD systems [9]. Given their potential to expedite and improve COVID-19 identification, ultimately facilitating timely and appropriate treatment interventions, CAD systems hold significant clinical value. Existing approaches for COVID-19 classification from CT scans can be broadly classified based on the type of feature descriptors extracted: traditional ML and deep learning (DL) techniques [10,11].

Conventional ML approaches for COVID-19 identification rely on meticulously crafted feature descriptors [12,13]. Conversely, DL models, specifically convolutional neural



**Citation:** Alinsaif, S. COVID-19 Image Classification: A Comparative Performance Analysis of Hand-Crafted vs. Deep Features. *Computation* **2024**, *1*, 0. <https://doi.org/>

Academic Editor: Anando Sen

Received: 4 March 2024

Revised: 28 March 2024

Accepted: 28 March 2024

Published: 30 March 2024



**Copyright:** © 2024 by the author. Licensee MDPI, Basel, Switzerland. This article is an open access article distributed under the terms and conditions of the Creative Commons Attribution (CC BY) license (<https://creativecommons.org/licenses/by/4.0/>).

networks (CNNs), offer the unique capability of end-to-end training [14,15]. However, their data-intensive nature necessitates substantial labeled data samples for training from scratch [16]. To circumvent this limitation, pre-trained CNN models can be fine-tuned and deployed as feature extractors, effectively capturing the salient information within medical images like CT scans [17].

Accurate and timely COVID-19 diagnosis presents a significant challenge in clinical settings. Robust automated detection methods can significantly aid medical professionals in making treatment decisions upon confirmation of the disease. This study, therefore, investigates a comprehensive range of feature descriptors for the classification of COVID-19 chest CT images. The primary objective is to identify a robust and efficient set of descriptors that accurately classify COVID-19 versus non-COVID-19 cases.

In the following, I provide a literature review of classification techniques for chest CT scans of patients afflicted with COVID-19 and outline this work's contributions.

## 2. Related Work

The automatic classification of COVID-19 CT images has garnered significant attention in recent research, as evidenced by a plethora of contributions documented in the literature [18–20]. In this section, I provide a review of these computer-aided system techniques, categorizing them into two distinct paradigms: traditional machine learning (TML) and deep learning (DL)-based approaches.

### 2.1. Traditional ML-Based Techniques

TML approaches for COVID-19 image classification typically adopt a pipelined structure. This workflow encompasses three key stages: (1) feature extraction, where relevant image characteristics (e.g., shape, color, texture) are isolated; (2) feature selection, which involves choosing a subset of informative features; and (3) classification model construction, where a model is trained to distinguish between COVID-19 and non-COVID-19 images. The ultimate goal is to achieve a robust classifier with minimal classification error. For instance, Hussain et al. [21] employed texture and morphological features to train various supervised classifiers for COVID-19 classification. Similarly, Chen et al. [22] utilized texture features derived from the Gray-Level Co-Occurrence Matrix (GLCM) to train a support vector machine (SVM) classifier within a 10-fold cross-validation (CV) framework.

Other studies have explored the utility of statistical moments for differentiating COVID-19 from non-COVID-19 images. Elaziz et al. [12] proposed the extraction of Fractional Multichannel Exponent Moments (FEMs) as features for classifier training. Their approach was evaluated on two independent datasets, achieving accuracies of 96.09% and 98.09%, respectively.

Ismael and Şengür [13] explored the efficacy of various multiresolution analysis techniques, namely wavelet, shearlet, and contourlet transforms, for COVID-19 detection in X-ray images. Following image decomposition, they extracted entropy and normalized entropy as features from the resulting subbands. These feature vectors were subsequently employed to train extreme learning machines (ELMs) for classification. The study utilized an imbalanced dataset comprising 200 healthy control samples and 361 COVID-19 X-ray images. The authors compared their proposed traditional method with the performance of DL-derived features. Interestingly, they concluded that traditional methods retain relevance and do not necessarily yield inferior results compared to DL approaches. This observation is supported by their finding that shearlet-based descriptors achieved an accuracy of 99.28%.

In a similar tendency to previous TML works, this research proposes to delve into a comprehensive exploration of hand-engineered descriptors. To mitigate the introduction of extraneous biases, the training and testing protocols will be held constant, while leveraging the identical COVID-19 dataset employed throughout the study.

## 2.2. DL-Based Techniques

In contrast to TML approaches, DL models offer the capability of end-to-end training directly on raw COVID-19 image data. The efficacy of DL architectures stems from their inherent capacity to autonomously acquire and unveil multi-tiered representations from data. Initial strata within the network typically concentrate on the extraction of fundamental characteristics, such as chromatic properties and boundaries [23]. Subsequently, higher strata progressively abstract these features, culminating in the formation of semantically significant representations of the input data. As an example, Ismael and Şengür [24] explored both fine-tuning pre-trained CNNs and training a CNN from scratch for COVID-19 detection in chest X-ray images. The utilized dataset comprised 180 COVID-19 and 200 healthy control X-ray images. The study evaluated various pre-trained models, including ResNet50, ResNet101, VGG16, and VGG19. Extracted deep features from these models were subsequently fed to an SVM for classification. The authors reported accuracies of 94.7%, 92.6%, and 91.6% for utilizing unsupervised deep features extraction, fine-tuning pre-trained models, and training from scratch, respectively.

Mirroring the approach of Ismael and Şengür [24], Haque et al. [25] investigated the utility of DL for COVID-19 detection in chest X-ray images. They explored both a custom-designed CNN model and fine-tuned pre-trained models (ResNet50, VGG-16, and VGG-19). Their proposed CNN architecture achieved an accuracy of 98.3% and a precision of 96.72%.

Furthermore, Jain et al. [26] investigated the use of X-ray images for COVID-19 detection through a DL model trained with data augmentation techniques. While their model was validated using a 5-fold CV scheme, it achieved an accuracy of 98.93%.

Saiz and Barandiaran [27] proposed an object detection DL architecture, which was trained and tested using publicly available datasets of 1500 images of normal and abnormal COVID-19 patients. The authors' primary goal was to classify the patients as infected or non-infected with COVID-19. The reported sensitivity and specificity were 94.92% and 92%, respectively.

Sahin et al. [28] investigated the application of DL methodologies for COVID-19 diagnosis utilizing CT imagery. Their approach leveraged Faster R-CNN and Mask R-CNN architectures for the classification of patients with COVID-19 and pneumonia. The study conducted a comparative analysis employing VGG-16 as the backbone for the Faster R-CNN model, while ResNet-50 and ResNet-101 backbones were utilized for the Mask R-CNN model. The implemented Faster R-CNN model achieved an accuracy of 93.86%. The Mask R-CNN model, employing ResNet-50 and ResNet-101 backbones, yielded mean average precision (mAP) values of 97.72% and 95.65%, respectively.

Avola et al. [29] investigated the effectiveness of twelve pre-trained DL models to differentiate between chest X-ray images from healthy individuals, those exhibiting signs of viral pneumonia (encompassing both generic and SARS-CoV-2 strains), and those with bacterial pneumonia. The experiment employed a dataset consisting of 6330 images, subdivided into training, validation, and testing sets. Standard classification metrics, such as precision and F1 scores, were computed for all models. The findings revealed that many of the implemented architectures achieved an average F1 score of up to 84.46% when distinguishing between the four designated classes.

Kathamuthu et al. [30] explored the efficacy of various deep transfer learning-based CNN architectures for the detection of COVID-19 in chest CT imagery. The investigation leverages pre-trained models including VGG16, VGG19, Densenet121, InceptionV3, Xception, and Resnet50 as foundational elements. The results demonstrate that the VGG16 model achieves superior performance within this study, attaining an accuracy of 98.00%.

Analogous to prior investigations documented within the literature, this study leverages established DL models; however, these models are employed solely for unsupervised feature extraction, eschewing fine-tuning. My approach focuses on utilizing the terminal layer within the network hierarchy, situated immediately before the classification layer. This selection is predicated on the assumption that these deep features encapsulate a semantic

representation of the input data. Notably, Nanni et al. [31] proposed a system that exploits features learned by CNNs across multiple levels. Their system advocates for the fusion of these learned features, subsequently leveraging them for various image classification tasks.

### 2.3. Contribution

Many computational techniques have been developed for the identification of COVID-19 using traditional and DL approaches. Many of these techniques lack standardized training and testing approaches. The importance of this research can be comprehended by answering the following questions:

- Why COVID-19 Detection is Still Important?
  - Long-Term Effects: COVID-19 can cause lingering health problems even after recovery. Thus, early detection potentially helps in managing these effectively.
  - Variants and Future Outbreaks: New variants can emerge, and having robust detection systems is indispensable for future outbreaks.
  - Improved Healthcare Systems: Coherent detection tools can minimize unnecessary hospitalizations and allocate resources better.
- Why a Comparative Study for COVID-19 is important?
  - Benchmarking Progress: Contrasting different techniques allows us to identify the well-performing models and track advancements in the field.
  - Understanding Best-Performing Methods: Knowing best-performing methods guides future development to generalize and adapt for other classification tasks in biomedicine.
  - Focus on Improving Techniques: Even if the overall trend of COVID-19 is decreasing, a comparative analysis of various techniques could potentially identify and improve robust techniques for COVID-19 detection.

Thus, I compute the performances while utilizing 27 descriptors on one popular COVID-19 dataset with the same experimental setting. Moreover, I compare the results achieved by handcrafted features with the results obtained by the state-of-the-art deep features. As such, a comparative experimental study was conducted on how well-advanced deep CNNs trained on ImageNet. To this end, I experimented with 12 deep networks that have different architectural designs and varying depths. These models are utilized as unsupervised feature extractors. As an advantage of using CNNs as unsupervised feature extractors, I avoid training and fine-tuning the models, and thus, fewer computational resources are needed. I also evaluate the robustness of both hand-crafted and deep features with an SVM, which is trained in the context of a 5-fold nested CV.

## 3. Methods

First and foremost, the progress and improvement in developing techniques related to the classification of COVID-19 chest CT scans are due to the public availability of such datasets. For instance, Angelov and Soares [32] is a highly cited paper that collected 2482 images of COVID-19 samples that I use in my investigation to evaluate and compare traditional and deep features techniques.

Machine learning [33] refers to the field of computer science where algorithms are trained to learn and solve problems from examples rather than being explicitly programmed. In the context of medical image analysis, particularly COVID-19, this involves building mathematical models based on datasets to achieve the task of differentiating between healthy vs diseased patients. These data-driven algorithms are constantly optimized through various optimization algorithms [34] to achieve high accuracy and efficiency in their performance. Ultimately, the goal is to develop a generalizable ML model that can accurately predict outcomes even for unseen data, meaning new medical images that are not included in the training dataset.

The construction of robust classifiers within a TML paradigm for COVID-19 image analysis hinges on the extraction of informative features from the data. Commonly utilized

features, as documented in the literature, include morphological descriptors, textural descriptors, and those derived from spectral methods. These extracted feature vectors subsequently serve as input to the classification model. As an alternative, DL approaches offer the distinct advantage of directly learning features from the raw medical images in an end-to-end manner, avoiding the feature extraction step. However, a notable limitation of DL techniques lies in their data-intensive nature, often requiring substantial labeled data samples for effective training from scratch.

A review of both traditional and DL-based techniques applied to COVID-19 patient datasets, as presented in the prior section, highlights their capability to achieve impressive classification performance. This suggests the potential of ML as a pre-screening tool to support radiologists in clinical settings. Notably, the literature indicates the efficacy of spectral methods, such as shearlet [35] and contourlet [36], coupled with statistical analysis for image analysis. The multiresolution and multi-scale nature of sub-bands obtained through image decomposition facilitates in-depth exploration. Notably, Ismael and Şengür [13] extracted shearlet coefficients and utilized entropy and normalized entropy as features, demonstrating the continued relevance of traditional methods.

My study addresses the challenge of limited medical data samples by evaluating and comparing various methods capable of mitigating this issue. I explore the performance of twenty-seven traditionally hand-crafted features. While DL methods have demonstrated promising classification results on diverse datasets, including those pertaining to COVID-19, they generally require substantial training data. To circumvent this limitation, a common practice in DL, particularly with scarce image samples, is to fine-tune a pre-trained model alongside data augmentation techniques to achieve optimal classification performance and avoid overfitting. In contrast, my approach investigates the use of DL models trained on non-medical image datasets (i.e., ImageNet [37]) as unsupervised feature extractors. My technique is implemented using MATLAB® 2021b. The experimental platform consisted of a computer system equipped with an Intel Core i7-9700 central processing unit (CPU) operating at a clock speed of 3.00 GHz. Additionally, the system was outfitted with an NVIDIA GeForce RTX 2080 graphics processing unit (GPU) possessing 8 GB of dedicated video memory.

### 3.1. Handcrafted Descriptors for COVID-19 Image Classification

Many conventional feature extraction methods aspire to detect a region of interest in images by computing geometric and appearance features [38], subsequently, these features are utilized to train traditional ML algorithms. Geometric features are computed based on the shape, locality of features, and salient points [39]. On the other hand, appearance-based attributes are based on texture information. In this study, I examine a set of 27 descriptors (MATLAB ToolboxDESC contains the implementation of 27 sets of descriptors that can be accessed via <https://github.com/cigdemturan/ToolboxDESC>, accessed on 1 January 2024) (as shown in Table 1). The same descriptors are utilized by Turan and Lam [38] to study facial expression recognition, but I examine these features to classify COVID-19 images.

**Table 1.** Details about the feature vector length of utilized hand-crafted features.

ID	Method	Abbreviation	Dimension
1	Binary Pattern of Phase Congruency [40]	BPPC	1062
2	Gradient Directional Pattern [41]	GDP	256
3	Gradient Direction Pattern [42]	GDP2	8
4	Gradient Local Ternary Pattern [43]	GLTeP	512
5	Improved Weber Binary Coding [44]	IWBC	2048
6	Local Arc Pattern [45]	LAP	272
7	Local Binary Pattern [46]	LBP	59
8	Local Directional Pattern [47]	LDiP	56
9	Local Directional Pattern Variance [48]	LDiPv	56
10	Local Directional Number Pattern [49]	LDN	56

Table 1. Cont.

ID	Method	Abbreviation	Dimension
11	Local Directional Texture Pattern [50]	LDTP	72
12	Local Frequency Descriptor [51]	LFD	512
13	Local Gabor Binary Pattern Histogram Sequence [52]	LGBPHS	256
14	Local Gabor Directional Pattern [53]	LGDiP	280
15	Local Gradient Increasing Pattern [54]	LGIP	37
16	Local Gradient Pattern [55]	LGP	7
17	Local Gabor Transitional Pattern [56]	LGTrP	256
18	Local Monotonic Pattern [57]	LMP	256
19	Local Phase Quantization [58]	LPQ	256
20	Local Ternary Pattern [59]	LTeP	512
21	Local Transitional Pattern [60]	LTrP	256
22	Monogenic Binary Coding [61]	MBC	3072
23	Median Binary Pattern [59]	MBP	256
24	Median Robust Extended Local Binary Pattern [62]	MRELBP	800
25	Median Ternary Pattern [59]	MTP	512
26	Pyramid of Histogram of Oriented Gradients [63]	PHOG	168
27	Weber Local Descriptor [64]	WLD	32

### 3.2. Deep Models for COVID-19 Images

Rather than training from scratch, I leverage pre-trained models capable of extracting meaningful features, i.e., these models are trained on vast datasets of non-medical images like ImageNet. These pre-trained models act as powerful but unsupervised feature extractors, generating deep features for COVID-19 image classification. Subsequently, I compare the performance of an SVM model trained and tested solely on these extracted features under a 5-fold nested CV scheme.

This study evaluates the capability of different CNN architectures to capture valuable information from COVID-19 images. I investigate both lightweight models like SqueezeNet 1.1 [65] and MobileNet v2 [66] for their efficiency, and larger models like ResNet-18 [67] and DenseNet-201 [68] for their potential in capturing richer details. Particularly, SqueezeNet utilizes diverse filter sizes to potentially extract both fine-grained and broader features from the images. MobileNet v2 boasts superior speed compared to other efficient models like ShuffleNet [69] and NASNet [70]. Notably, DenseNet-201 leverages feature reuse, where previously learned features are incorporated into subsequent layers, potentially enriching the information available for processing. In contrast, ResNet-18 employs element-wise addition to combine feature maps, offering a different approach to information flow.

My investigation encompassed the exploration of alternative DL models with comparable structures. Notably, Inception [71] exhibits similarities to DenseNet in its utilization of skip connections for depth-wise feature map concatenation. However, Inception's wider building block, constructed using diverse kernel sizes, resulted in subpar performance for COVID-19 image classification compared to DenseNet. Conversely, older models devoid of skip connections, such as VGG architectures [72], are susceptible to vanishing gradients and potentially slower training times. Nonetheless, My experimentation revealed promising results when applying these models to COVID-19 image classification.

A brief description of the CNN models that are used in this study is as follows.

- GoogLeNet (Inception) [73]: architecture relies on LeNet and AlexNet CNN models, but with the modification of depth and width of the layers. This model consists of 22 layers. It employs a parallel structure to significantly lessen the training time. As such, the model is designed to avoid patch-alignment problems by applying filter sizes of  $1 \times 1$ ,  $3 \times 3$ , and  $5 \times 5$ .
- Inception-ResNet-v2 [74]: model consists of 164 layers. This model relies on the family of Inception, but instead comprises residual connections. As such, this model replaces the filter concatenation step of the Inception CNN model.

- Inception-v3 [71]: comprising 48 layers, tackles the challenge of positional variance in salient image features by employing a multi-branch architecture. This architecture allows the network to incorporate diverse kernel types at the same level (sizes of  $1 \times 1$ ,  $3 \times 3$ , and pooling layers), effectively expanding the network's receptive field. These Inception modules enable the concurrent execution of numerous kernels, fostering greater feature extraction diversity. This core concept was introduced in the initial Inception-v1 model. Building upon its predecessor, Inception-v3 addresses the representational bottleneck issue through enhanced strategies. Notably, it incorporates kernel factorization and batch normalization within its auxiliary classifiers, leading to improved performance.
- VGG-16 and VGG-19 [72]: developed by the Visual Geometry Group (VGG) at the University of Oxford, VGG models represent a family of CNNs known for their simplicity and performance. Notably, VGG-16 and VGG-19, with 16 and 19 convolutional layers respectively, gained recognition at the ILSVRC 2014 competition as runners-up. These architectures feature relatively large numbers of parameters, with VGG-16 reaching approximately 138 million parameters. Additionally, both models incorporate fully connected layers containing 4096 hidden units each.
- SqueezeNet v1.1 [65]: network commences with a convolutional layer (conv1), followed by a sequence of eight blocks, each containing 2–9 fire modules. Each fire module employs a squeeze convolution layer with a filter size of  $1 \times 1$ , followed by two expand layers. One of these expand layers utilizes a filter size of  $1 \times 1$ , while the other utilizes a filter size of  $3 \times 3$ . The resulting feature maps from both expand layers are subsequently concatenated to form the input for the subsequent squeeze layer, which then feeds into the next fire module within the block.
- DenseNet-201 [68]: architecture leverages the concept of residual learning, introduced in ResNet, for network optimization. While ResNet employs element-wise addition of previous feature maps to the output, DenseNet utilizes depth concatenation of both the current and preceding outputs. This architecture comprises 32 dense blocks, each containing two distinct convolutional layers with kernel sizes of  $1 \times 1$  and  $3 \times 3$ , respectively. Notably, these convolutional layers are preceded by batch normalization for improved convergence and training stability.
- ResNet-18 [67]: architecture leverages a series of eight basic building blocks, each containing a sequence of two convolutional layers. These convolutional layers utilize a fixed filter size of  $3 \times 3$ , ensuring consistent spatial feature extraction. Critically, each convolutional layer is followed by batch normalization, a technique that facilitates faster convergence and improved training stability. Notably, a key mechanism of ResNet-18 lies in the residual connection. This involves the element-wise addition of the current block's output to the output of the preceding block, allowing the information flow to propagate efficiently through the network.
- ResNet-50 and ResNet-101 [67]: architectures comprise variations of the ResNet-18 model, differentiating themselves through their respective depths of 50 and 101 layers. Both architectures leverage the bottleneck residual module, which processes the input signal through two distinct branches: (1) Convolutional Processing Branch: This branch applies a series of convolutions with varying kernel sizes ( $1 \times 1$  and  $3 \times 3$ ) interspersed with batch normalization and ReLU activation functions; (2) Skip Connection Branch: This branch directly transmits the input signal unaltered, preserving crucial low-level feature information.
- Xception [75]: model stands out for its exclusive reliance on depthwise separable convolution layers. This architectural decision fosters computational efficiency while maintaining representational power. The network encompasses 36 convolutional layers, organized into 14 individual blocks. Only the first and final blocks deviate from the standard structure by lacking residual connections. In contrast, all remaining blocks incorporate linear residual connections. This strategic use of residual con-

nections facilitates gradient flow throughout the network, enhancing training and promoting optimal performance.

- MobileNet-v2 [66]: architecture incorporates two primary types of building blocks: (1) Linear Bottleneck Operations: These modules aim to achieve feature compression while maintaining representational power. (2) Skip Connections: These direct connections facilitate the flow of gradients and information across the network, mitigating the vanishing gradient problem that can occur in deep architectures. Both block types share fundamental operations, including convolution, batch normalization, and modified rectified linear unit (i.e.,  $\min(\max(x, 0), 6)$ ). The network comprises a total of 16 of these blocks, strategically arranged to achieve efficient feature extraction and classification performance.

#### *CNN as Feature Extractor*

The pre-trained CNN architectures, as detailed in Section 3.2, are utilized as unsupervised feature extractors. In this context, the deepest layer's output (directly preceding the classification layer) of each pre-trained model is flattened, generating a feature vector for each image. Fine-tuning of the pre-trained models is not conducted. Subsequently, a standard SVM classifier is trained and evaluated to assess the efficacy of these extracted deep features in classifying COVID-19 images. Table 2 presents a comprehensive overview of the feature vector lengths derived from each CNN model, thereby summarizing the salient features captured for each COVID-19 image.

**Table 2.** Details about the feature vector length of utilized CNN models as feature extractors.

Model's Name	Layer	Length
GoogLeNet	pool5-7x7_s1	1024
Inception-ResNet-v2	avg_pool	1536
Inception-v3	avg_pool	2048
VGG-16	fc6	4096
VGG-19	fc6	4096
ResNet-50	avg_pool	2048
ResNet-101	pool5	2048
SqueezeNet v1.1	pool10	1000
DenseNet-201	avg_pool	1920
ResNet-18	pool5	512
Xception	avg_pool	2048
MobileNet-v2	global_average_pooling2d_1	1280

## 4. Experiments and Results

This section provides a summary of the experiments conducted to evaluate and compare a wide range of hand-crafted and deep features for detecting COVID-19 infection from CT scan images. First, a description of the dataset utilized for the experimental studies is given at the beginning of this section. Then, a description of the nested cross-validation used to test my classification models and a list of utilized evaluation measures to assess the efficiency of the studied techniques. Followed by a brief highlight of the well-performing methods for the classification of COVID-19 CT images. Finally, I present a comprehensive review of the state-of-the-art methods with their corresponding performance utilizing the same benchmark dataset.

### 4.1. Dataset

For the purposes of this research investigation, I leverage the pre-processed COVID-19 dataset, SARS-CoV-2, as originally proposed by Angelov and Soares [32] and made publicly available on Kaggle ([www.kaggle.com/plameneduardo/sarscov2-ctscan-dataset](http://www.kaggle.com/plameneduardo/sarscov2-ctscan-dataset), accessed on 1 January 2024). This dataset contains a total of 2482 chest CT-scans images that belong either to COVID-19 (i.e., 1252 images) or non-COVID-19 (i.e., 1230 images). The CT scans

exhibit heterogeneity in their spatial dimensions, ranging from  $104 \times 119$  to  $416 \times 512$  pixels. Notably, all scans are grayscale and stored in the Portable Network Graphics (PNG) format. Angelov and Soares have classified the images based on the outcome of the RT-PCR tests. As such, patients with confirmed positive or negative RT-PCR tests for COVID-19 infection are included in the datasets.

#### 4.2. Nested Cross-Validation (CV)

This work employs a five-fold nested CV strategy for hyperparameter optimization. The dataset is partitioned into five equally sized subsets. Within each outer fold, an inner loop utilizes four subsets for training and hyperparameter tuning via a classifier. The remaining subset in the inner loop serves as the validation set for hyperparameter selection. The geometric mean of the classifier performance serves as the objective function for hyperparameter optimization within the inner loop. Upon convergence, the optimized classifier is evaluated on the test set of the outer fold, utilizing a range of performance metrics including accuracy, sensitivity, specificity, F-measure, area under the receiver operating characteristic curve, positive predictive value, negative predictive value, and the geometric mean. This process is repeated for each of the five outer folds, ensuring a robust estimation of the classifier's generalizability.

Following the five-fold nested CV protocol outlined previously, I reiterate the entire procedure five times. Subsequently, across these five iterations, the average of the following classification metrics [16] is reported:

- Accuracy  $ACC = (TP + TN)/(TP + TN + FP + FN)$ , where  $TP$ ,  $TN$ ,  $FP$ , and  $FN$  indicate the number of true positives, true negatives, false positives, and false negatives, respectively.
- Sensitivity  $SN = TP/(TP + FN)$ .
- Specificity  $SP = TN/(TN + FP)$ .
- F-Measure  $FM = (2 \times TP)/(2 \times TP + FP + FN)$
- The area under the curve ( $AUC$ ) encapsulates the relationship between the true positive rate (sensitivity) and the false positive rate ( $1 - \text{specificity}$ )
- Positive Predictive Value ( $PPV$ ) =  $TP/(TP + FP)$ .
- Negative Predictive Value ( $NPV$ ) =  $TN/(TN + FN)$ .
- Geometric mean ( $GM$ ) is the square root of the product of sensitivity and specificity, or  $GM = \sqrt{SN \times SP}$ .

#### 4.3. Results and Analysis

This section explores the classification results for COVID-19 detection. Initially, I present the performance of the SVM classifier utilizing hand-crafted descriptors. Subsequently, I report the SVM's performance when trained on diverse unsupervised deep features extracted from various CNN architectures. All built classification models in this study undergo training and validation within a nested CV framework.

##### 4.3.1. Classification Results Using Handcrafted Descriptors

This section investigates the classification performance of hand-crafted features extracted from the SARS-CoV-2 dataset for COVID-19 detection. Each sample undergoes summarization via 27 distinct techniques, with their corresponding feature vector lengths outlined in Table 1. Subsequently, the resulting feature matrix, where each row represents an image's feature vector and its associated label, is fed into an SVM classifier. As detailed in the nested CV section, a 5-fold nested CV scheme is employed to evaluate the classifier's performance, with the optimal model selected based on the geometric mean score (See Figure 1). Table 3 presents the classification results achieved by the SVM models utilizing various hand-engineered descriptors. Notably, the Pyramid of Histogram of Oriented Gradients (PHOG) exhibits the highest performance. Both Gradient Local Ternary Pattern (GLTeP) and Local Ternary Pattern (LTeP) achieve comparable results; however, PHOG

presents a distinct advantage due to its significantly lower feature vector dimensionality (168 compared to 512 for GLTeP and LTeP).

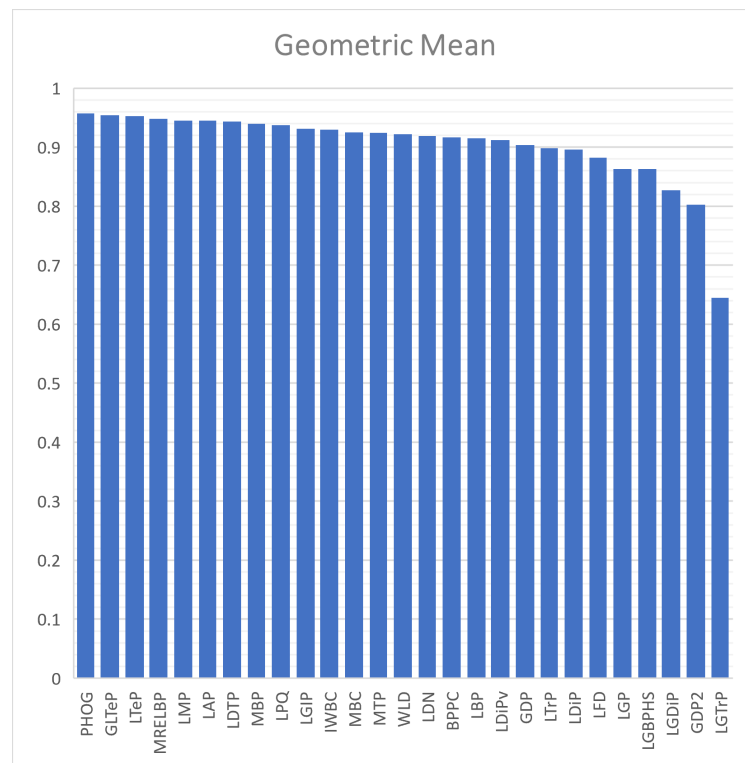


**Figure 1.** Achieved geometric mean by each hand-crafted method when used for training an SVM model in a 5-fold nested cross-validation fashion. Sorted from left to right.

**Table 3.** Average SVM performance trained using hand-engineered features for COVID-19 image classification. This table presents the mean values ± standard deviation.

ID	Method	ACC	SN	SP	FM	AUC	PPV	NPV	GM
1	BPPC	0.9175 ± 0.0104	0.9180 ± 0.0130	0.9171 ± 0.0202	0.9169 ± 0.0101	0.9175 ± 0.0103	0.9160 ± 0.0185	0.9194 ± 0.0113	0.9174 ± 0.0103
2	GDP	0.9045 ± 0.0245	0.8975 ± 0.0264	0.9114 ± 0.0251	0.9030 ± 0.0250	0.9045 ± 0.0245	0.9087 ± 0.0257	0.9007 ± 0.0251	0.9044 ± 0.0245
3	GDP2	0.8033 ± 0.0137	0.7990 ± 0.0173	0.8076 ± 0.0176	0.8010 ± 0.0137	0.8033 ± 0.0137	0.8031 ± 0.0152	0.8038 ± 0.0153	0.8032 ± 0.0137
4	GLTeP	0.9549 ± 0.0174	0.9508 ± 0.0123	0.9589 ± 0.0271	0.9544 ± 0.0171	0.9549 ± 0.0174	0.9583 ± 0.0263	0.9520 ± 0.0120	<b>0.9548 ± 0.0174</b>
5	IWBC	0.9301 ± 0.0235	0.9319 ± 0.0240	0.9284 ± 0.0231	0.9296 ± 0.0237	0.9301 ± 0.0235	0.9274 ± 0.0235	0.9329 ± 0.0236	0.9301 ± 0.0235
6	LAP	0.9456 ± 0.0192	0.9311 ± 0.0247	0.9598 ± 0.0180	0.9442 ± 0.0199	0.9454 ± 0.0192	0.9578 ± 0.0190	0.9344 ± 0.0228	0.9453 ± 0.0193
7	LBP	0.9155 ± 0.0228	0.9114 ± 0.0275	0.9195 ± 0.0188	0.9143 ± 0.0236	0.9155 ± 0.0229	0.9173 ± 0.0201	0.9138 ± 0.0258	0.9154 ± 0.0229
8	LDiP	0.8968 ± 0.0274	0.8868 ± 0.0229	0.9066 ± 0.0355	0.8950 ± 0.0270	0.8967 ± 0.0274	0.9036 ± 0.0344	0.8907 ± 0.0230	0.8966 ± 0.0273
9	LDiPv	0.9122 ± 0.0216	0.9212 ± 0.0202	0.9034 ± 0.0279	0.9123 ± 0.0211	0.9123 ± 0.0215	0.9038 ± 0.0259	0.9212 ± 0.0201	0.9122 ± 0.0216
10	LDN	0.9195 ± 0.0101	0.9033 ± 0.0181	0.9355 ± 0.0137	0.9175 ± 0.0096	0.9194 ± 0.0095	0.9323 ± 0.0136	0.9077 ± 0.0202	0.9192 ± 0.0095
11	LDTP	0.9439 ± 0.0143	0.9280 ± 0.0112	0.9594 ± 0.0192	0.9427 ± 0.0129	0.9437 ± 0.0141	0.9579 ± 0.0174	0.9308 ± 0.0157	0.9436 ± 0.0140
12	LFD	0.8826 ± 0.0180	0.8782 ± 0.0188	0.8872 ± 0.0247	0.8805 ± 0.0226	0.8827 ± 0.0181	0.8831 ± 0.0331	0.8816 ± 0.0145	0.8827 ± 0.0180
13	LGBPHS	0.8639 ± 0.0320	0.8496 ± 0.0395	0.8780 ± 0.0285	0.8602 ± 0.0359	0.8638 ± 0.0322	0.8713 ± 0.0367	0.8565 ± 0.0359	0.8636 ± 0.0322
14	LGDiP	0.8281 ± 0.0136	0.8323 ± 0.0123	0.8232 ± 0.0288	0.8273 ± 0.0148	0.8277 ± 0.0143	0.8225 ± 0.0229	0.8332 ± 0.0138	0.8276 ± 0.0145
15	LGIP	0.9313 ± 0.0136	0.9243 ± 0.0228	0.9389 ± 0.0115	0.9303 ± 0.0130	0.9316 ± 0.0135	0.9366 ± 0.0137	0.9258 ± 0.0259	0.9315 ± 0.0136
16	LGP	0.8639 ± 0.0151	0.8587 ± 0.0152	0.8690 ± 0.0181	0.8623 ± 0.0091	0.8638 ± 0.0150	0.8660 ± 0.0098	0.8611 ± 0.0270	0.8638 ± 0.0150
17	LGTrP	0.6477 ± 0.0303	0.5957 ± 0.0422	0.6987 ± 0.0205	0.6256 ± 0.0372	0.6472 ± 0.0302	0.6592 ± 0.0363	0.6379 ± 0.0408	0.6450 ± 0.0311
18	LMP	0.9455 ± 0.0151	0.9397 ± 0.0166	0.9515 ± 0.0162	0.9442 ± 0.0180	0.9456 ± 0.0154	0.9488 ± 0.0217	0.9420 ± 0.0123	0.9455 ± 0.0154
19	LPQ	0.9378 ± 0.0121	0.9249 ± 0.0173	0.9504 ± 0.0122	0.9359 ± 0.0154	0.9377 ± 0.0127	0.9474 ± 0.0172	0.9286 ± 0.0117	0.9376 ± 0.0128
20	LTeP	0.9529 ± 0.0160	0.9450 ± 0.0155	0.9606 ± 0.0176	0.9521 ± 0.0162	0.9528 ± 0.0160	0.9593 ± 0.0181	0.9468 ± 0.0150	<b>0.9528 ± 0.0160</b>
21	LTrP	0.8984 ± 0.0101	0.9026 ± 0.0154	0.8951 ± 0.0147	0.8976 ± 0.0131	0.8988 ± 0.0098	0.8931 ± 0.0227	0.9032 ± 0.0187	0.8988 ± 0.0098
22	MBC	0.9260 ± 0.0087	0.9102 ± 0.0151	0.9416 ± 0.0127	0.9237 ± 0.0129	0.9259 ± 0.0096	0.9378 ± 0.0179	0.9148 ± 0.0097	0.9257 ± 0.0096
23	MBP	0.9403 ± 0.0062	0.9374 ± 0.0142	0.9428 ± 0.0106	0.9394 ± 0.0077	0.9401 ± 0.0062	0.9415 ± 0.0111	0.9391 ± 0.0124	0.9400 ± 0.0063
24	MRELBP	0.9496 ± 0.0092	0.9124 ± 0.0229	0.9854 ± 0.0081	0.9468 ± 0.0121	0.9489 ± 0.0104	0.9842 ± 0.0084	0.9207 ± 0.0153	0.9481 ± 0.0108
25	MTP	0.9252 ± 0.0049	0.9077 ± 0.0115	0.9418 ± 0.0113	0.9230 ± 0.0075	0.9247 ± 0.0053	0.9389 ± 0.0097	0.9126 ± 0.0049	0.9245 ± 0.0053
26	PHOG	0.9581 ± 0.0049	0.9490 ± 0.0129	0.9670 ± 0.0098	0.9572 ± 0.0063	0.9580 ± 0.0053	0.9658 ± 0.0094	0.9510 ± 0.0111	<b>0.9579 ± 0.0054</b>
27	WLD	0.9228 ± 0.0106	0.9139 ± 0.0064	0.9317 ± 0.0160	0.9213 ± 0.0116	0.9228 ± 0.0105	0.9289 ± 0.0193	0.9165 ± 0.0115	0.9228 ± 0.0104

Top-3 best-performing hand-crafted methods are highlighted.

An unpaired *t*-test was conducted to investigate the statistical distinction between PHOG and GLTeP in their performance on the SARS-CoV-2 classification task. The test

revealed that there is no statistically significant difference ( $p < 0.05$ ), with a two-tailed  $p$ -value of 0.7135 and a  $t$ -value of 0.3805.

### 4.3.2. Classification Results Using Deep Features

This section leverages the SARS-CoV-2 dataset for my investigation. Each image within the dataset is processed through various pre-trained CNN models. Table 2 summarizes the feature vector lengths extracted from each of these CNN architectures. Subsequently, the resulting feature matrix, where each row represents an image’s feature vector and its corresponding label, is fed into an SVM classifier. The performance of my classifier is evaluated using a 5-fold nested CV scheme, following the hyperparameter optimization strategy outlined in the nested CV section. The optimal model is chosen based on the geometric mean score (See Figure 2). As presented in Table 4, the deep features extracted from DenseNet-201 yield the highest classification performance. Notably, VGG-16 achieves comparable results to DenseNet-201.

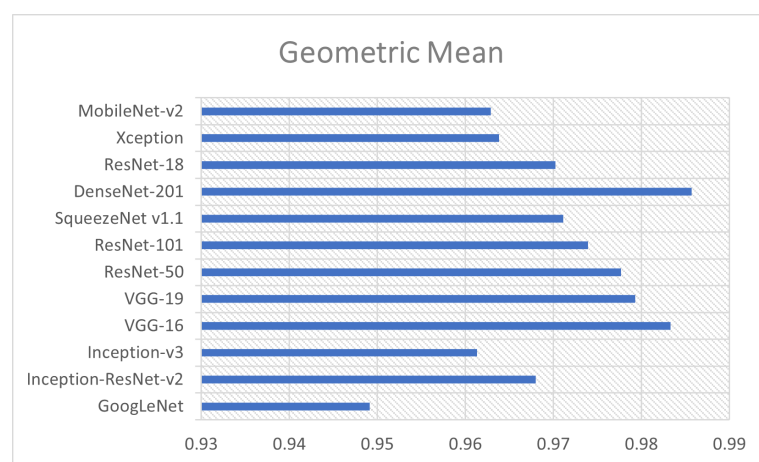


**Figure 2.** Achieved geometric mean by each CNN model’s deep features when used for training an SVM model in a 5-fold nested cross-validation fashion.

**Table 4.** Average SVM performance trained using deep features for COVID-19 image classification. This table presents the mean values ± standard deviation.

Model’s Name	ACC	SN	SP	FM	AUC	PPV	NPV	GM
GoogLeNet	0.9533 ± 0.0069	0.9475 ± 0.0090	0.9589 ± 0.0128	0.9526 ± 0.0069	0.9532 ± 0.0069	0.9579 ± 0.0126	0.9491 ± 0.0080	0.9491 ± 0.0080
Inception-ResNet-v2	0.9679 ± 0.0062	0.9672 ± 0.0127	0.9686 ± 0.0105	0.9676 ± 0.0063	0.9679 ± 0.0062	0.9681 ± 0.0100	0.9680 ± 0.0118	0.9680 ± 0.0118
Inception-v3	0.9614 ± 0.0092	0.9622 ± 0.0163	0.9606 ± 0.0164	0.9611 ± 0.0094	0.9614 ± 0.0092	0.9602 ± 0.0157	0.9632 ± 0.0152	0.9613 ± 0.0092
VGG-16	0.9833 ± 0.0048	0.9787 ± 0.0089	0.9879 ± 0.0090	0.9831 ± 0.0050	0.9833 ± 0.0049	0.9877 ± 0.0090	0.9793 ± 0.0084	<b>0.9833 ± 0.0049</b>
VGG-19	0.9821 ± 0.0049	0.9787 ± 0.0111	0.9855 ± 0.0105	0.9819 ± 0.0050	0.9821 ± 0.0049	0.9853 ± 0.0105	0.9793 ± 0.0103	0.9793 ± 0.0103
ResNet-50	0.9809 ± 0.0045	0.9770 ± 0.0074	0.9847 ± 0.0112	0.9807 ± 0.0044	0.9809 ± 0.0044	0.9844 ± 0.0111	0.9777 ± 0.0069	0.9777 ± 0.0069
ResNet-101	0.9768 ± 0.0018	0.9729 ± 0.0147	0.9807 ± 0.0138	0.9765 ± 0.0020	0.9768 ± 0.0018	0.9805 ± 0.0134	0.9739 ± 0.0137	0.9739 ± 0.0137
SqueezeNet v1.1	0.9712 ± 0.0098	0.9655 ± 0.0085	0.9767 ± 0.0149	0.9707 ± 0.0099	0.9711 ± 0.0097	0.9761 ± 0.0151	0.9666 ± 0.0081	0.9711 ± 0.0097
DenseNet-201	0.9858 ± 0.0029	0.9819 ± 0.0085	0.9895 ± 0.0073	0.9856 ± 0.0029	0.9857 ± 0.0029	0.9893 ± 0.0073	0.9825 ± 0.0080	<b>0.9857 ± 0.0029</b>
ResNet-18	0.9703 ± 0.0118	0.9655 ± 0.0160	0.9750 ± 0.0164	0.9699 ± 0.0119	0.9703 ± 0.0118	0.9745 ± 0.0164	0.9667 ± 0.0151	0.9702 ± 0.0118
Xception	0.9638 ± 0.0062	0.9664 ± 0.0034	0.9614 ± 0.0147	0.9636 ± 0.0059	0.9639 ± 0.0061	0.9611 ± 0.0143	0.9668 ± 0.0029	0.9638 ± 0.0061
MobileNet-v2	0.9630 ± 0.0075	0.9590 ± 0.0157	0.9670 ± 0.0112	0.9625 ± 0.0077	0.9630 ± 0.0075	0.9663 ± 0.0108	0.9603 ± 0.0144	0.9629 ± 0.0076

Top-2 best-performing set of deep features are highlighted.

To assess the statistical difference between DenseNet-201 and VGG-16 on the SARS-CoV-2 classification task, I performed an unpaired  $t$ -test. The results yielded no statistically significant difference ( $p < 0.05$ ), with a two-tailed  $p$ -value equal to 0.3735 and a  $t$ -statistic of 0.9425.

### 4.4. Discussion

The landscape of COVID-19 classification using publicly available datasets, such as the SARS-CoV-2 dataset [32], is rapidly evolving. Researchers have proposed diverse conventional and DL techniques for classifying COVID-19 from CT-scan images. How-

ever, objective comparison across studies remains challenging due to several key factors impacting framework performance. These factors include: (1) Heterogeneity in CT-scan selection: Variations in acquisition protocols, scanners, and patient populations across datasets can significantly impact feature extraction and model generalization. (2) Varied image pre-processing techniques: Different pre-processing approaches, such as noise reduction, normalization, and segmentation, can significantly influence the extracted features and subsequent classification performance. (3) Divergence in training/testing protocols: Variations in data splitting (e.g., k-fold cross-validation, train/test ratio), evaluation metrics, and hyperparameter tuning strategies can hinder direct performance comparisons. Acknowledging these influencing factors is crucial for interpreting and comparing the results of COVID-19 classification studies.

A case study conducted by Maguolo and Nanni [76] examined various testing protocols while using COVID-19 X-ray 2D images. The authors showed that similar classification performance can be achieved while training a neural network using X-ray images that do not contain most of the lungs. Maguolo and Nanni removed the lungs from the images by inserting a black box into the center of the X-ray image. Then, these new images were used for training their classifiers only on the outer part of the images. The authors concluded that many of the testing protocols of published studies in the literature are not fair and the classifiers of neural networks were not learning patterns related to COVID-19. Hence, rigorous testing protocols should be established while training a DL model. As a result, one can conclude that assessing and comparing the performance of a method objectively is difficult because it is not clear which part of the technique (e.g., feature extraction/selection, pre-processing, or classification models) led to a tangible enhancement. Thus, my aim in my study is to learn from available published studies and to avoid potential mistakes (e.g., learning from the recommendation of Maguolo and Nanni to test with unbiased testing protocols).

Subsequently, I objectively planned to minimize the bias of the dataset by selecting SARS-CoV-2 dataset and this dataset is divided in the context of 5-fold nested cross-validation to rigorously evaluate wide range of hand-crafted descriptors and deep features from different number of CNN architectures, as shown in Tables 3 and 4. There are a large number of studies that utilized the SARS-CoV-2 dataset from which ten studies are summarized indicating their methodology essence, their training/testing protocol, and reported classification performance. Noteworthy, there is a vast number of studies that used the same dataset [30,77–98], but of similar nature, and thus, these studies are not summarized. Here is the summary of the ten studies:

- Halder and Datta [99] investigated the efficacy of transfer learning employing pre-trained CNN models, namely DenseNet201, VGG16, ResNet50V2, and MobileNet. Each model was independently trained and tested with a ratio of 8:2 on both unmodified and augmented datasets. Notably, DenseNet201 exhibited exceptional performance, achieving an AUC of 1.00 and 0.99 for the unaugmented and augmented datasets, respectively. Moreover, training DenseNet201 with the augmented data yielded a test set accuracy of 97%, surpassing ResNet50V2 (96%), MobileNet (95%), and VGG16 (94%).
- Alshazly et al. [100] investigated the application of transfer learning to various pre-trained CNN architectures, including SqueezeNet, Inception, ResNet, ResNeXt, Xception, ShuffleNet, and DenseNet. Five-fold cross-validation was utilized to evaluate the efficacy of their approach. Their ResNet101 model demonstrated remarkable performance, achieving average accuracy, precision, sensitivity, specificity, and F1-score values of 99.4%, 99.6%, 99.1%, 99.6%, and 99.4%, respectively.
- Ragab et al. [101] proposed a multi-modal fusion architecture for COVID-19 image classification. Their system leverages the pre-trained CNNs, namely AlexNet, GoogleNet, ShuffleNet, and ResNet-18, alongside hand-crafted features derived from statistical analysis, discrete wavelet transform, and grey-level co-occurrence matrix. They employed five-fold cross-validation to evaluate the efficacy of their approach. This

hybrid methodology achieved performance, attaining an average accuracy, sensitivity, specificity, and precision of approximately 99% across all evaluation metrics.

- Shaik and Cherukuri [102] presented an ensemble learning approach for COVID-19 image classification that leverages the combined prediction of diverse pre-trained CNN architectures. They employ a collection of eight models, including VGG16, VGG19, InceptionV3, ResNet50, ResNet50V2, InceptionResNetV2, Xception, and MobileNet. Each model is fine-tuned using an 80/20 data split for training and validation, respectively. This ensemble approach achieved an accuracy of 98.99%, precision of 98.98%, recall of 99.00%, and F-measure of 98.99%.
- Gaur et al. [103] presented a method that leverages the spectral information within each image channel (red, green, and blue) by applying a 2D-empirical wavelet transform. This decomposition generates five frequency sub-bands, which are subsequently augmented to enhance data variability. These augmented sub-bands then serve as the input for training a DenseNet121 classification model. To ensure a statistically robust evaluation, the dataset was randomly split into 1000 training, 100 validation, and 152 testing images prior to data augmentation. This strategy yielded a performance of accuracy of 85.50%, F-measure of 85.28%, and AUC of 96.6%.
- Canayaz et al. [104] explores the efficacy of Bayesian optimization in enhancing the performance of various machine learning algorithms for COVID-19 image classification. The authors propose and evaluate the application of this optimization technique to MobilNetv2, ResNet-50, SVM, and k-nearest neighbor (kNN) models. The proposed method consists of three steps: (1) train and optimize the deep learning models, (2) utilize trained models as feature extractors, and (3) train a machine learning algorithm. Notably, the ResNet-50 architecture, when optimized via Bayesian optimization and employed as a feature extractor for kNN (trained on 1968 COVID-19 images and tested on 492), yielded an accuracy of 99.37%, accompanied by a precision of 99.38%, recall of 99.36%, and F-score of 99.37%.
- Attallah and Samir [105] presented a two-stage framework for COVID-19 image classification that leverages spectral-temporal and spatial information. In the first stage, their method employs discrete wavelet decomposition (DWT) to extract frequency-domain features from the images, represented as heatmaps. These features are subsequently used to train a ResNet CNN model. Simultaneously, the original images are utilized to train a separate ResNet CNN model, capturing spatial information. Subsequently, both pipelines converge in a feature fusion stage, where spectral-temporal features are integrated with spatial features extracted from the second ResNet. To address dimensionality, the combined feature set is subjected to dimensionality reduction before being fed into support vector machine (SVM) classifiers. This strategy achieved a classification accuracy of 99.7% under a 5-fold cross-validation scheme.
- Kundu et al. [106] explored an ensemble learning approach by leveraging transfer learning. Their method, employing bootstrap aggregating (bagging) of three pre-trained architectures Inception v3, ResNet34, and DenseNet201 were examined under a 5-fold cross-validation scheme. The ensemble model achieved an accuracy of 97.81%, precision of 97.77%, sensitivity (recall) of 97.81%, and specificity of 97.77%.
- Islam and Nahiduzzaman [107] proposed employing a custom CNN architecture for extracting deep features. These features are subsequently fed into traditional machine learning algorithms, encompassing Gaussian Naive Bayes, Support Vector Machine, Decision Tree, Logistic Regression, and Random Forest. The output of these five learning algorithms is ensembled to find the final prediction. The proposed model undergoes training on 2109 COVID-19 images and evaluation on a separate set of 373 images. The model achieved an accuracy of 99.73%, an F1-score of 99.73%, a recall of 100%, and a precision of 99.46%.
- Choudhary et al. [108] introduced an approach for COVID-19 detection on resource-constrained devices, focusing on “important weights-only” transfer learning. This method optimizes pre-trained deep learning models for deployment on point-of-care

devices by selectively pruning less essential weight parameters. Their experiments were conducted on VGG16 and ResNet34 architectures. The proposed method was evaluated while using 1,687 samples for training, 420 samples for validation, and 375 samples for testing. The pruned ResNet34 model achieved an accuracy of 95.47%, a sensitivity of 0.9216, an F1-score of 0.9567, and a specificity of 0.9942 while exhibiting reductions in computational requirements: 41.96% fewer floating-point operations and 20.64% fewer weight parameters compared to the unpruned model.

It is noteworthy that the application of DL techniques has become predominant in SARS-CoV-2 research. Researchers often leverage various CNN architectures, opting for fine-tuning with or without data augmentation to address the inherent scarcity of medical datasets. While impressive results have been reported, inconsistencies in training and validation strategies across studies pose challenges for objective comparison. In contrast, my approach utilizes unsupervised deep features, minimizing computational demands. Furthermore, I employ a rigorous 5-fold nested CV scheme to evaluate the performance of my SVM classification models.

## 5. Conclusions and Future Studies

The main goal of this work is to compare and evaluate a wide range of conventional and DL-based techniques to identify effective and efficient approaches for classifying COVID-19 disease from CT scans. To achieve this goal, twenty-seven conventional techniques and 12 CNN architectures are examined. Thereafter each set of descriptors is fed as input to an SVM model, which is tested in the context of a 5-fold cross-validation scheme. The performance of the proposed methodologies is evaluated on the SARS-CoV-2 dataset. The empirical findings gleaned from this investigation posit that the proposed method holds promise for adoption as a pre-screening tool for COVID-19 cases, exhibiting competitive performance in comparison to established state-of-the-art methodologies. Additionally, the establishment of my framework requires minimal computational resources for conventional techniques, and particularly, for DL-based techniques as I avoid fine-tuning and data augmentation.

In the future, I plan to test my approach using other datasets with a similar nature of complexity, for example, the COVID-CT (COVID-CT benchmark can be accessed via <https://www.kaggle.com/datasets/hgunraj/covidxct>, accessed on 1 January 2024) dataset [109] and COVID multiclass dataset (The COVID-19 multiclass dataset can be accessed via <https://www.kaggle.com/datasets/plameneduardo/a-covid-multiclass-dataset-of-ct-scans>, accessed on 1 January 2024). Furthermore, I plan to combine both hand-crafted and deep features [110] in an attempt to deliver more robust classification models.

**Funding:** This research received no external funding.

**Institutional Review Board Statement:** Not applicable.

**Data Availability Statement:** This research leverages a publicly available dataset. COVID-19 dataset, SARS-CoV-2, can be accessed on Kaggle [www.kaggle.com/plameneduardo/sarscov2-ctscan-dataset](http://www.kaggle.com/plameneduardo/sarscov2-ctscan-dataset), accessed on 1 January 2024.

**Conflicts of Interest:** The author declares no conflict of interest.

## References

1. Liu, J.; Liao, X.; Qian, S.; Yuan, J.; Wang, F.; Liu, Y.; Wang, Z.; Wang, F.S.; Liu, L.; Zhang, Z. Community transmission of severe acute respiratory syndrome coronavirus 2, Shenzhen, China, 2020. *Emerg. Infect. Dis.* **2020**, *26*, 1320. [[CrossRef](#)] [[PubMed](#)]
2. Ghinai, I.; McPherson, T.D.; Hunter, J.C.; Kirking, H.L.; Christiansen, D.; Joshi, K.; Rubin, R.; Morales-Estrada, S.; Black, S.R.; Pacilli, M.; et al. First known person-to-person transmission of severe acute respiratory syndrome coronavirus 2 (SARS-CoV-2) in the USA. *Lancet* **2020**, *395*, 1137–1144. [[CrossRef](#)] [[PubMed](#)]
3. Morens, D.M.; Fauci, A.S. Emerging pandemic diseases: How we got to COVID-19. *Cell* **2020**, *182*, 1077–1092. [[CrossRef](#)] [[PubMed](#)]
4. Poudel, A.N.; Zhu, S.; Cooper, N.; Roderick, P.; Alwan, N.; Tarrant, C.; Ziauddeen, N.; Yao, G.L. Impact of COVID-19 on health-related quality of life of patients: A structured review. *PLoS ONE* **2021**, *16*, e0259164. [[CrossRef](#)]

5. Arevalo-Rodriguez, I.; Buitrago-Garcia, D.; Simancas-Racines, D.; Zambrano-Achig, P.; Del Campo, R.; Ciapponi, A.; Sued, O.; Martinez-Garcia, L.; Rutjes, A.W.; Low, N.; et al. False-negative results of initial RT-PCR assays for COVID-19: A systematic review. *PLoS ONE* **2020**, *15*, e0242958. [[CrossRef](#)] [[PubMed](#)]
6. Axiac, A.; Almohtadi, A.; Massias, S.A.; Ngemoh, D.; Harky, A. The role of computed tomography scan in the diagnosis of COVID-19 pneumonia. *Curr. Opin. Pulm. Med.* **2021**, *27*, 163–168. [[CrossRef](#)] [[PubMed](#)]
7. Fang, Y.; Zhang, H.; Xie, J.; Lin, M.; Ying, L.; Pang, P.; Ji, W. Sensitivity of chest CT for COVID-19: Comparison to RT-PCR. *Radiology* **2020**, *296*, E115–E117. [[CrossRef](#)] [[PubMed](#)]
8. Ai, T.; Yang, Z.; Hou, H.; Zhan, C.; Chen, C.; Lv, W.; Tao, Q.; Sun, Z.; Xia, L. Correlation of chest CT and RT-PCR testing for coronavirus disease 2019 (COVID-19) in China: A report of 1014 cases. *Radiology* **2020**, *296*, E32–E40. [[CrossRef](#)] [[PubMed](#)]
9. Hassan, H.; Ren, Z.; Zhao, H.; Huang, S.; Li, D.; Xiang, S.; Kang, Y.; Chen, S.; Huang, B. Review and classification of AI-enabled COVID-19 CT imaging models based on computer vision tasks. *Comput. Biol. Med.* **2022**, *141*, 105123. [[CrossRef](#)]
10. Saygili, A. A new approach for computer-aided detection of coronavirus (COVID-19) from CT and X-ray images using machine learning methods. *Appl. Soft Comput.* **2021**, *105*, 107323. [[CrossRef](#)] [[PubMed](#)]
11. Shi, F.; Wang, J.; Shi, J.; Wu, Z.; Wang, Q.; Tang, Z.; He, K.; Shi, Y.; Shen, D. Review of artificial intelligence techniques in imaging data acquisition, segmentation, and diagnosis for COVID-19. *IEEE Rev. Biomed. Eng.* **2020**, *14*, 4–15. [[CrossRef](#)] [[PubMed](#)]
12. Elaziz, M.A.; Hosny, K.M.; Salah, A.; Darwish, M.M.; Lu, S.; Sahlol, A.T. New machine learning method for image-based diagnosis of COVID-19. *PLoS ONE* **2020**, *15*, e0235187. [[CrossRef](#)] [[PubMed](#)]
13. Ismael, A.M.; Şengür, A. The investigation of multiresolution approaches for chest X-ray image based COVID-19 detection. *Health Inf. Sci. Syst.* **2020**, *8*, 29. [[CrossRef](#)]
14. Alam, M.; Akram, M.U.; Fareed, W. Deep Learning-based Analysis and Classification of COVID Patients Through CT Images. In Proceedings of the IEEE 2023 3rd International Conference on Artificial Intelligence (ICAI), Wuhan, China, 17–19 November 2023; pp. 136–141.
15. Reis, H.C.; Turk, V. COVID-DSNet: A novel deep convolutional neural network for detection of coronavirus (SARS-CoV-2) cases from CT and Chest X-Ray images. *Artif. Intell. Med.* **2022**, *134*, 102427. [[CrossRef](#)] [[PubMed](#)]
16. Alinsaif, S. Unraveling Arrhythmias with Graph-Based Analysis: A Survey of the MIT-BIH Database. *Computation* **2024**, *12*, 21. [[CrossRef](#)]
17. Özkaya, U.; Öztürk, Ş.; Barstugan, M. Coronavirus (COVID-19) classification using deep features fusion and ranking technique. In *Big Data Analytics and Artificial Intelligence Against COVID-19: Innovation Vision and Approach*; Springer: Cham, Switzerland, 2020; pp. 281–295.
18. Rahmani, A.M.; Azhir, E.; Naserbakht, M.; Mohammadi, M.; Aldalwie, A.H.M.; Majeed, M.K.; Taher Karim, S.H.; Hosseinzadeh, M. Automatic COVID-19 detection mechanisms and approaches from medical images: A systematic review. *Multimed. Tools Appl.* **2022**, *81*, 28779–28798. [[CrossRef](#)] [[PubMed](#)]
19. Benameur, N.; Mahmoudi, R.; Zaid, S.; Arous, Y.; Hmida, B.; Bedoui, M.H. SARS-CoV-2 diagnosis using medical imaging techniques and artificial intelligence: A review. *Clin. Imaging* **2021**, *76*, 6–14. [[CrossRef](#)] [[PubMed](#)]
20. Serena Low, W.C.; Chuah, J.H.; Tee, C.A.T.; Anis, S.; Shoaib, M.A.; Faisal, A.; Khalil, A.; Lai, K.W. An overview of deep learning techniques on chest X-ray and CT scan identification of COVID-19. *Comput. Math. Methods Med.* **2021**, *2021*, 5528144. [[CrossRef](#)] [[PubMed](#)]
21. Hussain, L.; Nguyen, T.; Li, H.; Abbasi, A.A.; Lone, K.J.; Zhao, Z.; Zaib, M.; Chen, A.; Duong, T.Q. Machine-learning classification of texture features of portable chest X-ray accurately classifies COVID-19 lung infection. *BioMed. Eng. Online* **2020**, *19*, 88. [[CrossRef](#)] [[PubMed](#)]
22. Chen, Y. COVID-19 classification based on gray-level co-occurrence matrix and support vector machine. In *COVID-19: Prediction, Decision-Making, and Its Impacts*; Springer: Singapore, 2021; pp. 47–55.
23. Yosinski, J.; Clune, J.; Bengio, Y.; Lipson, H. How transferable are features in deep neural networks? In Proceedings of the Advances in Neural Information Processing Systems, Montreal, QC, Canada, 8–13 December 2014; Volume 27.
24. Ismael, A.M.; Şengür, A. Deep learning approaches for COVID-19 detection based on chest X-ray images. *Expert Syst. Appl.* **2021**, *164*, 114054. [[CrossRef](#)]
25. Haque, K.F.; Abdelgawad, A. A deep learning approach to detect COVID-19 patients from chest X-ray images. *AI* **2020**, *1*, 27. [[CrossRef](#)]
26. Jain, G.; Mittal, D.; Thakur, D.; Mittal, M.K. A deep learning approach to detect COVID-19 coronavirus with X-Ray images. *Biocybern. Biomed. Eng.* **2020**, *40*, 1391–1405. [[CrossRef](#)] [[PubMed](#)]
27. Saiz, F.; Barandiaran, I. COVID-19 detection in chest X-ray images using a deep learning approach. *Int. J. Interact. Multimed. Artif. Intell.* **2020**. [[CrossRef](#)]
28. Sahin, M.E.; Ulutas, H.; Yuce, E.; Erkoc, M.F. Detection and classification of COVID-19 by using faster R-CNN and mask R-CNN on CT images. *Neural Comput. Appl.* **2023**, *35*, 13597–13611. [[CrossRef](#)] [[PubMed](#)]
29. Avola, D.; Bacciu, A.; Cinque, L.; Fagioli, A.; Marini, M.R.; Taiello, R. Study on transfer learning capabilities for pneumonia classification in chest-x-rays images. *Comput. Methods Programs Biomed.* **2022**, *221*, 106833. [[CrossRef](#)] [[PubMed](#)]
30. Kathamuthu, N.D.; Subramaniam, S.; Le, Q.H.; Muthusamy, S.; Panchal, H.; Sundararajan, S.C.M.; Alrubaie, A.J.; Zahra, M.M.A. A deep transfer learning-based convolution neural network model for COVID-19 detection using computed tomography scan images for medical applications. *Adv. Eng. Softw.* **2023**, *175*, 103317. [[CrossRef](#)] [[PubMed](#)]

31. Nanni, L.; Ghidoni, S.; Brahmam, S. Deep features for training support vector machines. *J. Imaging* **2021**, *7*, 177. [[CrossRef](#)] [[PubMed](#)]
32. Angelov, P.; Almeida Soares, E. SARS-CoV-2 CT-scan dataset: A large dataset of real patients CT scans for SARS-CoV-2 identification. *MedRxiv* **2020**. [[CrossRef](#)]
33. Britain, R.S.G. *Machine Learning: The Power and Promise of Computers That Learn by Example: An Introduction*; Royal Society: London, UK, 2017.
34. Shawe-Taylor, J.; Sun, S. A review of optimization methodologies in support vector machines. *Neurocomputing* **2011**, *74*, 3609–3618. [[CrossRef](#)]
35. Kutyniok, G.; Labate, D. Introduction to shearlets. In *Shearlets: Multiscale Analysis for Multivariate Data*; Springer: New York, NY, USA, 2012; pp. 1–38.
36. Do, M.N.; Vetterli, M. The contourlet transform: An efficient directional multiresolution image representation. *IEEE Trans. Image Process.* **2005**, *14*, 2091–2106. [[CrossRef](#)] [[PubMed](#)]
37. Deng, J.; Dong, W.; Socher, R.; Li, L.J.; Li, K.; Fei-Fei, L. Imagenet: A large-scale hierarchical image database. In Proceedings of the 2009 IEEE Conference on Computer Vision and Pattern Recognition, Miami, FL, USA, 20–25 June 2009; pp. 248–255.
38. Turan, C.; Lam, K.M. Histogram-based local descriptors for facial expression recognition (FER): A comprehensive study. *J. Vis. Commun. Image Represent.* **2018**, *55*, 331–341. [[CrossRef](#)]
39. Sebe, N.; Tian, Q.; Loupias, E.; Lew, M.S.; Huang, T.S. Evaluation of salient point techniques. *Image Vis. Comput.* **2003**, *21*, 1087–1095. [[CrossRef](#)]
40. Shojaeilangari, S.; Yau, W.Y.; Li, J.; Teoh, E.K. Feature extraction through binary pattern of phase congruency for facial expression recognition. In Proceedings of the 2012 12th International Conference on Control Automation Robotics & Vision (ICARCV), Guangzhou, China, 5–7 December 2012; pp. 166–170.
41. Ahmed, F. Gradient directional pattern: A robust feature descriptor for facial expression recognition. *Electron. Lett.* **2012**, *48*, 1203–1204. [[CrossRef](#)]
42. Islam, M.S. Gender classification using gradient direction pattern. *Sci. Int.* **2013**, *25*, 797–799.
43. Valstar, M.; Pantic, M. Fully automatic facial action unit detection and temporal analysis. In Proceedings of the IEEE 2006 Conference on Computer Vision and Pattern Recognition Workshop (CVPRW'06), New York, NY, USA, 17–22 June 2006; p. 149.
44. Yang, B.Q.; Zhang, T.; Gu, C.C.; Wu, K.J.; Guan, X.P. A novel face recognition method based on IWLD and IWBC. *Multimed. Tools Appl.* **2016**, *75*, 6979–7002. [[CrossRef](#)]
45. Islam, M.S.; Auwatanamo, S. Facial expression recognition using local arc pattern. *Trends Appl. Sci. Res.* **2014**, *9*, 113. [[CrossRef](#)]
46. Ojala, T.; Pietikainen, M.; Maenpaa, T. Multiresolution gray-scale and rotation invariant texture classification with local binary patterns. *IEEE Trans. Pattern Anal. Mach. Intell.* **2002**, *24*, 971–987. [[CrossRef](#)]
47. Jabid, T.; Kabir, M.H.; Chae, O. Local directional pattern (LDP)—A robust image descriptor for object recognition. In Proceedings of the 2010 7th IEEE International Conference on Advanced Video and Signal Based Surveillance, Boston, MA, USA, 29 August–1 September 2010; pp. 482–487.
48. Kabir, M.H.; Jabid, T.; Chae, O. A local directional pattern variance (LDPv) based face descriptor for human facial expression recognition. In Proceedings of the 2010 7th IEEE International Conference on Advanced Video and Signal Based Surveillance, Boston, MA, USA, 29 August–1 September 2010; pp. 526–532.
49. Rivera, A.R.; Castillo, J.R.; Chae, O.O. Local directional number pattern for face analysis: Face and expression recognition. *IEEE Trans. Image Process.* **2012**, *22*, 1740–1752. [[CrossRef](#)] [[PubMed](#)]
50. Rivera, A.R.; Castillo, J.R.; Chae, O. Local directional texture pattern image descriptor. *Pattern Recognit. Lett.* **2015**, *51*, 94–100. [[CrossRef](#)]
51. Lei, Z.; Ahonen, T.; Pietikainen, M.; Li, S.Z. Local frequency descriptor for low-resolution face recognition. In Proceedings of the 2011 IEEE International Conference on Automatic Face & Gesture Recognition (FG), Santa Barbara, CA, USA, 21–23 March 2011; pp. 161–166.
52. Zhang, W.; Shan, S.; Gao, W.; Chen, X.; Zhang, H. Local gabor binary pattern histogram sequence (lgbphs): A novel non-statistical model for face representation and recognition. In Proceedings of the 10th IEEE International Conference on Computer Vision (ICCV'05), Washington, DC, USA, 17–20 October 2005; Volume 1, pp. 786–791.
53. Ishraque, S.Z.; Banna, A.H.; Chae, O. Local Gabor directional pattern for facial expression recognition. In Proceedings of the 2012 IEEE 15th International Conference on Computer and Information Technology (ICCIT), Chittagong, Bangladesh, 22–24 December 2012; pp. 164–167.
54. Zhou, L.; Wang, H. Local gradient increasing pattern for facial expression recognition. In Proceedings of the 2012 19th IEEE International Conference on Image Processing, Orlando, FL, USA, 30 September–3 October 2012; pp. 2601–2604.
55. Islam, M.S. Local gradient pattern—A novel feature representation for facial expression recognition. *J. AI Data Min.* **2014**, *2*, 33–38.
56. Ahsan, T.; Jabid, T.; Chong, U.P. Facial expression recognition using local transitional pattern on Gabor filtered facial images. *IETE Tech. Rev.* **2013**, *30*, 47–52. [[CrossRef](#)]
57. Mohammad, T.; Ali, M.L. Robust facial expression recognition based on local monotonic pattern (LMP). In Proceedings of the 14th International Conference on Computer and Information Technology (ICCIT 2011), Dhaka, Bangladesh, 22–24 December 2011; pp. 572–576.

58. Ojansivu, V.; Heikkilä, J. Blur insensitive texture classification using local phase quantization. In Proceedings of the Image and Signal Processing: 3rd International Conference (ICISP 2008), Cherbourg-Octeville, France, 1–3 July 2008; Springer: Berlin/Heidelberg, Germany, 2008; pp. 236–243.
59. Bashar, F.; Khan, A.; Ahmed, F.; Kabir, M.H. Robust facial expression recognition based on median ternary pattern (MTP). In Proceedings of the IEEE 2013 International Conference on Electrical Information and Communication Technology (EICT), Khulna, Bangladesh, 13–15 February 2014; pp. 1–5.
60. Jabid, T.; Chae, O. Local transitional pattern: A robust facial image descriptor for automatic facial expression recognition. In Proceedings of the International Conference on Computer Convergence Technology, Seoul, Republic of Korea, 28–30 September 2011; pp. 333–344.
61. Lu, J.; Liong, V.E.; Zhou, J. Cost-sensitive local binary feature learning for facial age estimation. *IEEE Trans. Image Process.* **2015**, *24*, 5356–5368. [[CrossRef](#)] [[PubMed](#)]
62. Liu, L.; Lao, S.; Fieguth, P.W.; Guo, Y.; Wang, X.; Pietikäinen, M. Median robust extended local binary pattern for texture classification. *IEEE Trans. Image Process.* **2016**, *25*, 1368–1381. [[CrossRef](#)] [[PubMed](#)]
63. Bosch, A.; Zisserman, A.; Munoz, X. Representing shape with a spatial pyramid kernel. In Proceedings of the 6th ACM International Conference on Image and Video Retrieval, Amsterdam, The Netherlands, 9–11 July 2007; pp. 401–408.
64. Li, S.; Gong, D.; Yuan, Y. Face recognition using Weber local descriptors. *Neurocomputing* **2013**, *122*, 272–283. [[CrossRef](#)]
65. Iandola, F.N.; Han, S.; Moskewicz, M.W.; Ashraf, K.; Dally, W.J.; Keutzer, K. SqueezeNet: AlexNet-level accuracy with 50x fewer parameters and < 0.5 MB model size. *arXiv* **2016**, arXiv:1602.07360.
66. Sandler, M.; Howard, A.; Zhu, M.; Zhmoginov, A.; Chen, L.C. Mobilenetv2: Inverted residuals and linear bottlenecks. In Proceedings of the IEEE Conference on Computer Vision and Pattern Recognition, Salt Lake City, UT, USA, 18–22 June 2018; pp. 4510–4520.
67. He, K.; Zhang, X.; Ren, S.; Sun, J. Deep residual learning for image recognition. In Proceedings of the IEEE Conference on Computer Vision and Pattern Recognition, Las Vegas, NV, USA, 27–30 June 2016; pp. 770–778.
68. Huang, G.; Liu, Z.; Van Der Maaten, L.; Weinberger, K.Q. Densely connected convolutional networks. In Proceedings of the IEEE Conference on Computer Vision and Pattern Recognition, Honolulu, HI, USA, 21–26 July 2017; pp. 4700–4708.
69. Zhang, X.; Zhou, X.; Lin, M.; Sun, J. Shufflenet: An extremely efficient convolutional neural network for mobile devices. In Proceedings of the IEEE Conference on Computer Vision and Pattern Recognition, Salt Lake City, UT, USA, 18–22 June 2018; pp. 6848–6856.
70. Zoph, B.; Vasudevan, V.; Shlens, J.; Le, Q.V. Learning transferable architectures for scalable image recognition. In Proceedings of the IEEE Conference on Computer Vision and Pattern Recognition, Salt Lake City, UT, USA, 18–22 June 2018; pp. 8697–8710.
71. Szegedy, C.; Vanhoucke, V.; Ioffe, S.; Shlens, J.; Wojna, Z. Rethinking the inception architecture for computer vision. In Proceedings of the IEEE Conference on Computer Vision and Pattern Recognition, Las Vegas, NV, USA, 27–30 June 2016; pp. 2818–2826.
72. Simonyan, K.; Zisserman, A. Very deep convolutional networks for large-scale image recognition. *arXiv* **2014**, arXiv:1409.1556.
73. Szegedy, C.; Liu, W.; Jia, Y.; Sermanet, P.; Reed, S.; Anguelov, D.; Erhan, D.; Vanhoucke, V.; Rabinovich, A. Going deeper with convolutions. In Proceedings of the IEEE Conference on Computer Vision and Pattern Recognition, Boston, MA, USA, 7–12 June 2015; pp. 1–9.
74. Szegedy, C.; Ioffe, S.; Vanhoucke, V.; Alemi, A. Inception-v4, inception-resnet and the impact of residual connections on learning. In Proceedings of the AAAI Conference on Artificial Intelligence, San Francisco, CA, USA, 4–9 February 2017; Volume 31.
75. Chollet, F. Xception: Deep learning with depthwise separable convolutions. In Proceedings of the IEEE Conference on Computer Vision and Pattern Recognition, Honolulu, HI, USA, 21–26 July 2017; pp. 1251–1258.
76. Maguolo, G.; Nanni, L. A critic evaluation of methods for covid-19 automatic detection from x-ray images. *Inf. Fusion* **2021**, *76*, 1–7. [[CrossRef](#)] [[PubMed](#)]
77. Aswathy, A.; Hareendran, A.; SS, V.C. COVID-19 diagnosis and severity detection from CT-images using transfer learning and back propagation neural network. *J. Infect. Public Health* **2021**, *14*, 1435–1445.
78. Li, C.; Yang, Y.; Liang, H.; Wu, B. Transfer learning for establishment of recognition of COVID-19 on CT imaging using small-sized training datasets. *Knowl.-Based Syst.* **2021**, *218*, 106849. [[CrossRef](#)] [[PubMed](#)]
79. Lahsaini, I.; Daho, M.E.H.; Chikh, M.A. Deep transfer learning based classification model for COVID-19 using chest CT-scans. *Pattern Recognit. Lett.* **2021**, *152*, 122–128. [[CrossRef](#)]
80. Pinki, F.T.; Masud, M.A.; Ferdousi, J.; Eva, F.Y.; Rana, M.M.R. SVM Based COVID-19 Detection from CT Scan Image using Local Feature. In Proceedings of the IEEE 2021 International Conference on Electronics, Communications and Information Technology (ICECIT), Online, 14–16 September 2021; pp. 1–4.
81. Kaur, T.; Gandhi, T.K. Classifier fusion for detection of COVID-19 from CT scans. *Circuits Syst. Signal Process.* **2022**, *41*, 3397–3414. [[CrossRef](#)]
82. Islam, M.K.; Habiba, S.U.; Khan, T.A.; Tasnim, F. COV-RadNet: A Deep Convolutional Neural Network for Automatic Detection of COVID-19 from Chest X-rays and CT Scans. *Comput. Methods Programs Biomed. Update* **2022**, *2*, 100064. [[CrossRef](#)] [[PubMed](#)]
83. Peng, L.; Wang, C.; Tian, G.; Liu, G.; Li, G.; Lu, Y.; Yang, J.; Chen, M.; Li, Z. Analysis of CT scan images for COVID-19 pneumonia based on a deep ensemble framework with DenseNet, Swin transformer, and RegNet. *Front. Microbiol.* **2022**, *13*, 995323. [[CrossRef](#)] [[PubMed](#)]

84. Singh, V.K.; Kolekar, M.H. Deep learning empowered COVID-19 diagnosis using chest CT scan images for collaborative edge-cloud computing platform. *Multimed. Tools Appl.* **2022**, *81*, 3–30. [[CrossRef](#)] [[PubMed](#)]
85. DOLMA, Ö. COVID-19 and Non-COVID-19 Classification from Lung CT-Scan Images Using Deep Convolutional Neural Networks. *Int. J. Multidiscip. Stud. Innov. Technol.* **2023**, *7*, 53–60. [[CrossRef](#)]
86. Tiwari, S.; Jain, A.; Chawla, S.K. Diagnosing COVID-19 From Chest CT Scan Images Using Deep Learning Models. *Int. J. Reliab. Qual. e-Healthc. (IJRQEH)* **2022**, *11*, 1–15. [[CrossRef](#)]
87. Premamayudu, B.; Bhuvaneshwari, C. COVID-19 Automatic Detection from CT Images through Transfer Learning. *Int. J. Image Graph. Signal Process.* **2022**, *14*, 48–95. [[CrossRef](#)]
88. Zahir, M.J.B.; Azim, M.A.; Chy, A.N.; Islam, M.K. A Fast and Reliable Approach for COVID-19 Detection from CT-Scan Images. *J. Inf. Syst. Eng. Bus. Intell.* **2023**, *9*, 288–304. [[CrossRef](#)]
89. Ibrahim, W.R.; Mahmood, M.R. Classified COVID-19 by densenet121-based deep transfer learning from CT-scan images. *Sci. J. Univ. Zakho* **2023**, *11*, 571–580. [[CrossRef](#)]
90. Ibrahim, M.R.; Youssef, S.M.; Fathalla, K.M. Abnormality detection and intelligent severity assessment of human chest computed tomography scans using deep learning: A case study on SARS-COV-2 assessment. *J. Ambient. Intell. Humaniz. Comput.* **2023**, *14*, 5665–5688. [[CrossRef](#)] [[PubMed](#)]
91. Gupta, K.; Bajaj, V. Deep learning models-based CT-scan image classification for automated screening of COVID-19. *Biomed. Signal Process. Control* **2023**, *80*, 104268. [[CrossRef](#)] [[PubMed](#)]
92. Duong, L.T.; Nguyen, P.T.; Iovino, L.; Flammini, M. Automatic detection of COVID-19 from chest X-ray and lung computed tomography images using deep neural networks and transfer learning. *Appl. Soft Comput.* **2023**, *132*, 109851. [[CrossRef](#)] [[PubMed](#)]
93. Ali, N.G.; El Sheref, F.K. A Hybrid Model for COVID-19 Detection using CT-Scans. *Int. J. Adv. Comput. Sci. Appl.* **2023**, *14*, 627–633. [[CrossRef](#)]
94. Farjana, A.; Liza, F.T.; Al Mamun, M.; Das, M.C.; Hasan, M.M. SARS CovidAID: Automatic detection of SARS CoV-19 cases from CT scan images with pretrained transfer learning model (VGG19, RESNet50 and DenseNet169) architecture. In Proceedings of the IEEE 2023 International Conference on Smart Applications, Communications and Networking (SmartNets), Istanbul, Turkey, 25–27 July 2023; pp. 1–6.
95. Lim, Y.J.; Lim, K.M.; Lee, C.P.; Chang, R.K.Y.; Lim, J.Y. COVID-19 identification and analysis with CT scan images using densenet and support vector machine. In Proceedings of the IEEE 2023 11th International Conference on Information and Communication Technology (ICOICT), Melaka, Malaysia, 23–24 August 2023; pp. 254–259.
96. Motwani, A.; Shukla, P.K.; Pawar, M.; Kumar, M.; Ghosh, U.; Alnumay, W.; Nayak, S.R. Enhanced framework for COVID-19 prediction with computed tomography scan images using dense convolutional neural network and novel loss function. *Comput. Electr. Eng.* **2023**, *105*, 108479. [[CrossRef](#)] [[PubMed](#)]
97. Perumal, M.; Srinivas, M. DenSplitnet: Classifier-invariant neural network method to detect COVID-19 in chest CT data. *J. Vis. Commun. Image Represent.* **2023**, *97*, 103949. [[CrossRef](#)]
98. Krishnan, A.; Rajesh, S.; Gollapinni, K.; Mohan, M.; Srinivasa, G. A Comparative Analysis of Chest X-rays and CT Scans Towards COVID-19 Detection. In Proceedings of the IEEE 2023 4th International Conference for Emerging Technology (INCET), Belgaum, India, 26–28 May 2023; pp. 1–7.
99. Halder, A.; Datta, B. COVID-19 detection from lung CT-scan images using transfer learning approach. *Mach. Learn. Sci. Technol.* **2021**, *2*, 045013. [[CrossRef](#)]
100. Alshazly, H.; Linse, C.; Barth, E.; Martinetz, T. Explainable COVID-19 detection using chest CT scans and deep learning. *Sensors* **2021**, *21*, 455. [[CrossRef](#)]
101. Ragab, D.A.; Attallah, O. FUSI-CAD: Coronavirus (COVID-19) diagnosis based on the fusion of CNNs and handcrafted features. *PeerJ Comput. Sci.* **2020**, *6*, e306. [[CrossRef](#)]
102. Shaik, N.S.; Cherukuri, T.K. Transfer learning based novel ensemble classifier for COVID-19 detection from chest CT-scans. *Comput. Biol. Med.* **2022**, *141*, 105127. [[CrossRef](#)] [[PubMed](#)]
103. Gaur, P.; Malaviya, V.; Gupta, A.; Bhatia, G.; Pachori, R.B.; Sharma, D. COVID-19 disease identification from chest CT images using empirical wavelet transformation and transfer learning. *Biomed. Signal Process. Control* **2022**, *71*, 103076. [[CrossRef](#)]
104. Canayaz, M.; Şehribanoğlu, S.; Özdağ, R.; Demir, M. COVID-19 diagnosis on CT images with Bayes optimization-based deep neural networks and machine learning algorithms. *Neural Comput. Appl.* **2022**, *34*, 5349–5365. [[CrossRef](#)] [[PubMed](#)]
105. Attallah, O.; Samir, A. A wavelet-based deep learning pipeline for efficient COVID-19 diagnosis via CT slices. *Appl. Soft Comput.* **2022**, *128*, 109401. [[CrossRef](#)]
106. Kundu, R.; Singh, P.K.; Ferrara, M.; Ahmadian, A.; Sarkar, R. ET-NET: An ensemble of transfer learning models for prediction of COVID-19 infection through chest CT-scan images. *Multimed. Tools Appl.* **2022**, *81*, 31–50. [[CrossRef](#)] [[PubMed](#)]
107. Islam, M.R.; Nahiduzzaman, M. Complex features extraction with deep learning model for the detection of COVID19 from CT scan images using ensemble based machine learning approach. *Expert Syst. Appl.* **2022**, *195*, 116554. [[CrossRef](#)] [[PubMed](#)]
108. Choudhary, T.; Gujar, S.; Goswami, A.; Mishra, V.; Badal, T. Deep learning-based important weights-only transfer learning approach for COVID-19 CT-scan classification. *Appl. Intell.* **2023**, *53*, 7201–7215. [[CrossRef](#)]

109. Gunraj, H.; Wang, L.; Wong, A. Covidnet-ct: A tailored deep convolutional neural network design for detection of covid-19 cases from chest ct images. *Front. Med.* **2020**, *7*, 608525. [[CrossRef](#)] [[PubMed](#)]
110. Alinsaif, S.; Lang, J. 3D shearlet-based descriptors combined with deep features for the classification of Alzheimer's disease based on MRI data. *Comput. Biol. Med.* **2021**, *138*, 104879. [[CrossRef](#)] [[PubMed](#)]

**Disclaimer/Publisher's Note:** The statements, opinions and data contained in all publications are solely those of the individual author(s) and contributor(s) and not of MDPI and/or the editor(s). MDPI and/or the editor(s) disclaim responsibility for any injury to people or property resulting from any ideas, methods, instructions or products referred to in the content.